Journal of the European Ceramic Society **15** (1995) 939–950
© 1995 Elsevier Science Limited
Printed in Great Britain. All rights reserved
0955-2219/95/$9.50

0955-2219(95)00063-1

Effect of Solid Solution Additives on the Sintering of Ultra-fine CeO_2 Powders

M. N. Rahaman[a] & Y. C. Zhou[b]

[a]University of Missouri–Rolla, Department of Ceramic Engineering, Rolla, Missouri 65401, USA
[b]Institute of Metal Research, Academia Sinica, Shenyang 110015, P. R. China

(Received 12 September 1994; revised 6 March 1995; accepted 10 March 1995)

Abstract

Ultra-fine CeO_2 powders (particle size ≈10–15 nm) containing up to 20 at% of various divalent and trivalent cations (Mg^{2+}, Ca^{2+}, Sc^{3+}, Y^{3+} and Nd^{3+}) were prepared by chemical precipitation under hydrothermal conditions. The effects of the cation concentration, size and valency on the densification and grain growth of the compacted powders were examined during sintering at a constant heating rate of 10°C/min. Compared to undoped CeO_2, all of the additive cations caused a shift in the densification curve to higher temperatures. However, the density and grain size achieved after sintering depended significantly on the elemental composition of the additive. When the radii of the additive cations were larger than that of the host Ce^{4+} cation, (i.e. Ca^{2+}, Y^{3+} and Nd^{3}), nearly full density and ultra-fine grain size were achieved. Under identical sintering conditions, lower density (≈93–95% of the theoretical) and larger grain size were achieved when the radii of the additive cations were smaller than that of the host, (i.e. Mg^{2+} and Sc^{3+}). Powders doped simultaneously with two cations, (e.g. Ca^{2+} and Mg^{2+}) showed sintering and grain growth characteristics which were intermediate between those for the powders doped with single cations at the equivalent concentration.

1 Introduction

Materials with ultra-fine grained microstructure (sometimes referred to as nanocrystalline materials) have been the subject of much recent investigation.[1–8] While considerable attention has been devoted towards the preparation of ultra-fine particles and the production of thin films by vapor phase or sol–gel techniques, the production of bulk materials with controlled density and grain size by the sintering of ultra-fine particles has received little attention. Due to their ultra-fine size, typically of the order of 10 nm or so, nanocrystalline powders have a fairly large fraction of molecules residing in the surface of the particles. Nanocrystalline solids also contain a large number of grain boundaries per unit volume. The consequences of these characteristics for sintering and grain growth have not been determined.

An understanding of the sintering behavior of ultra-fine powders is also important for the application of nanocrystalline materials. The driving force for densification increases and the diffusion distance for matter transport decreases with a decrease in the particle size. From the point of view of materials fabrication, a key benefit of ultra-fine powders, therefore, is the reduction in the sintering temperature. Many properties are dependent on the grain size of the fabricated body. Another key benefit is the production of ultra-fine grained microstructures. Such microstructures are of great practical interest for the investigation of structure–property relationships in polycrystalline materials. A problem is that non-densifying processes such as vapor transport and surface diffusion are also enhanced with a decrease in the particle size.[9] These processes lead to coarsening of the microstructure and, consequently, to the reduction in the driving force for densification. The benefits of the ultra-fine particle size for sintering are therefore not clear.

The reduction in the sintering temperature of ultra-fine powders has been observed in a number of studies.[3,7,8] However, the production, by sintering, of materials with high density and ultra-fine microstructure has experienced difficulties. Rapid grain growth in the final stage of sintering has been a common problem so that the achievement of high density has normally been accompanied by relatively large grain size.[3,7]

In an earlier study, the present authors investigated the sintering of ultra-fine CeO_2 powders which were prepared under hydrothermal conditions.[10] Nearly full density and ultra-fine grain size (less than ≈200 nm) were obtained by careful control of the heating schedule or with the use of powders doped with yttrium. The present paper describes a more detailed study of the preparation and sintering of doped, ultra-fine CeO_2 powders. The effects of substituting cations differing in valency and ionic size were investigated. Of particular interest was the effect of the additive cations on the morphology and chemical homogeneity of the synthesized powders and on the sintering and grain growth of the compacted powders. CeO_2 was considered to be a useful model system for these studies because of its relatively simple cubic fluorite crystal structure[11] and its high solid solubility for many cations.[12] In addition, it does not undergo any known crystallographic transformation during the normal range of heating. The results are expected to be relevant to the general understanding of the sintering behavior of ultra-fine powders and to the elucidation of the role of dopants in sintering. Solid solutions of CeO_2 have also been attracting considerable interest as solid electrolytes with high ionic conductivity for applications in fuel cells.[13,14] The present study may also be useful for the microstructure control of CeO_2 solid electrolytes.

2 Experimental

2.1 Hydrothermal synthesis of CeO_2 powders and doped CeO_2 powders

Powders of undoped CeO_2 and of solid solutions of CeO_2 containing up to 20 at% of Mg, Ca, Sc, Y and Nd were prepared by hydrothermal techniques. The starting materials for the preparation of the powders consisted of Analar Grade nitrate or chloride salts of the appropriate metals with a purity greater than 99.9%: cerium (III) nitrate hexahydrate,* $Ce(NO_3)_3.6H_2O$, magnesium nitrate hexahydrate,† $Mg(NO_3)_2.6H_2O$, calcium nitrate tetrahydrate,† $Ca(NO_3)_2.4H_2O$, scandium nitrate hexahydrate,† $Sc(NO_3)_3.6H_2O$, yttrium chloride hexahydrate,* $YCl_3,6H_2O$, and neodymium nitrate hexahydrate,† $Nd(NO_3)_3.6H_2O$.

In the hydrothermal synthesis of the powders, the appropriate amounts of cerium nitrate (for the undoped CeO_2) or a mixture of cerium nitrate and the desired metal salt, (e.g. yttrium chloride, for the CeO_2 solid solution containing yttrium) were dissolved in distilled water and ammonium hydroxide solution was added, under vigorous stirring, to produce a sol at pH = 10. The gelatinous precipitate was filtered, washed with distilled water and then transferred to a Teflon tube which was sealed with a cap and placed in an autoclave. Hydrothermal synthesis was performed for 4 h at ≈300°C and under a pressure of ≈10 MPa. After rapid cooling, the product was washed with distilled water, dried in air at room temperature and then ground lightly in an agate mortar and pestle. Finally, the powder was calcined at 200°C for 2 h. The preparation conditions were kept almost identical for each powder composition.

2.2 Sintering of the compacted powders

Powder compacts (6 mm diameter by 4 mm) were formed by uniaxial pressing in a die at ≈50 MPa in a tungsten carbide die. The compacts were sintered in air in a dilatometer which allowed continuous monitoring of the shrinkage kinetics. The sample holder and pushrods of the dilatometer were made of high purity alumina. Sintering was performed at a constant heating rate of 10°C/min to 1350–1400°C. The density of the sample at any temperature was determined from the initial density and the measured shrinkage. The final density was checked by Archimedes' method.

2.3 Characterization of the powders and sintered materials

The ultra-fine powders prepared by hydrothermal synthesis were characterized by X-ray diffraction (XRD), thermogravimetric analysis (TGA), differential thermal analysis (DTA) and transmission electron microscopy (TEM). The TGA and DTA analyses were performed at a heating rate of 10°C/min. Analysis of the crystal structure of the powder was performed in a diffractometer (Scintag XDS 2000) using Cu K_α radiation at a scan rate of 2° 2θ min^{-1}. Crystallite size was measured from XRD patterns at a scan rate of 0·5° 2θ min^{-1}. The crystallite size, H, was calculated from the Scherer formula:

$$H = \frac{0{\cdot}9\ \lambda}{\beta \cos \theta} \tag{1}$$

where λ is the wavelength of the X-rays, θ is the diffraction angle, and β is the corrected half width given by:

$$\beta^2 = \beta_m^2 - \beta_s^2 \tag{2}$$

where β_m is the measured half width and β_s is the half width of a standard CeO_2 sample with a crystal size greater than 100 nm. The reflection from the (422) plane, occurring at 88° 2θ, was used for the crystallite size measurement.

Transmission electron microscopy was also used to characterize the powders. Samples were prepared by dispersing the powder in ethanol and then putting a drop of the suspension on a holey

---

*Aldrich Chemical Co., Milwaukee, WI, USA; †Johnson Matthey, Seabrook, NH, USA.

carbon film and allowing it to dry. The microstructure of the powders was observed in a Philips EM-420 transmission electron microscope. In addition, the microstructure of the CeO_2 powders doped with Y and Ca was observed in a JEOL-2000FXII high resolution electron microscope. The distribution of the dopants in the doped powders were analyzed by energy dispersive X-ray analysis (EDX).

The microstructure of the sintered samples was observed using scanning electron microscopy (SEM) of fracture surfaces. The grain size was measured by the line intercept method. The microstructure of selected samples were also observed in a JEOL-2000FXII high resolution electron microscope. The samples for TEM were prepared by cutting to a thickness of ≈0·5 mm, followed by mechanical polishing to ≈25 μm and finally ion beam milling at 5 kV using an incident angle of 15°. Phase composition of the sintered materials was analyzed by XRD of powder samples at a scan rate of $2° \, 2\theta \, \mathrm{min}^{-1}$.

3 Results

The results of the present work allowed an investigation of the effects of solid solution additives on the sintering of compacted CeO_2 powders. Since the characteristics of the synthesized powder can have a significant influence on the sintering behavior, it is important to determine how these characteristics are controlled by the concentration and elemental composition of the additive. Figure 1 shows the effect of dopant concentration on the characteristics of the powder doped with yttrium. The TEM micrographs show powders of undoped CeO_2 (a), and CeO_2 doped with Y^{3+} at concentrations of 6 at% (b), 10 at% (c) and 20 at% (d). The undoped CeO_2 powder consists of polyhedral shaped particles with an average size of ≈12 nm (as measured by X-ray line broadening). The average size measured by TEM was ≈14 nm, which agrees well with the value obtained by X-ray line broadening. The powders doped with 10 and 20 at% yttrium have an average size and shape that are close to that for the undoped powder. However, the powder containing 6 at% Y^{3+} shows a fairly significant difference in size. The average particle size obtained from X-ray line broadening measurements for the powder doped with 6 at% Y^{3+} was 9 nm.

The effect of the elemental composition of the dopant on the characteristics of the synthesized powder is shown in Fig. 2 for undoped CeO_2 powder (a) and for doped CeO_2 powder containing

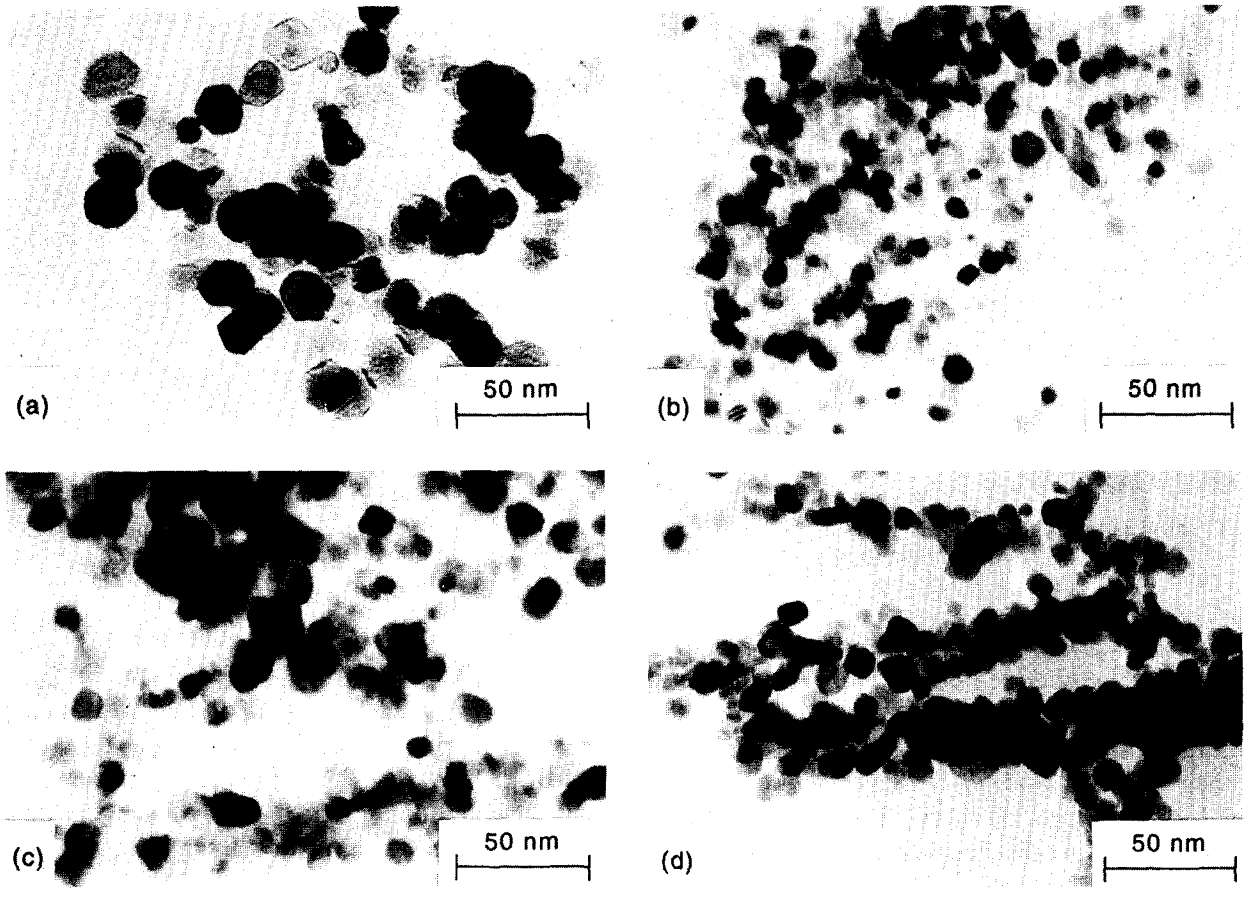

Fig. 1. TEM of the CeO_2 powder doped with Y^{3+} at concentrations of (a) 0; (b) 6; (c) 10 and (d) 20 at% prepared under hydrothermal conditions.

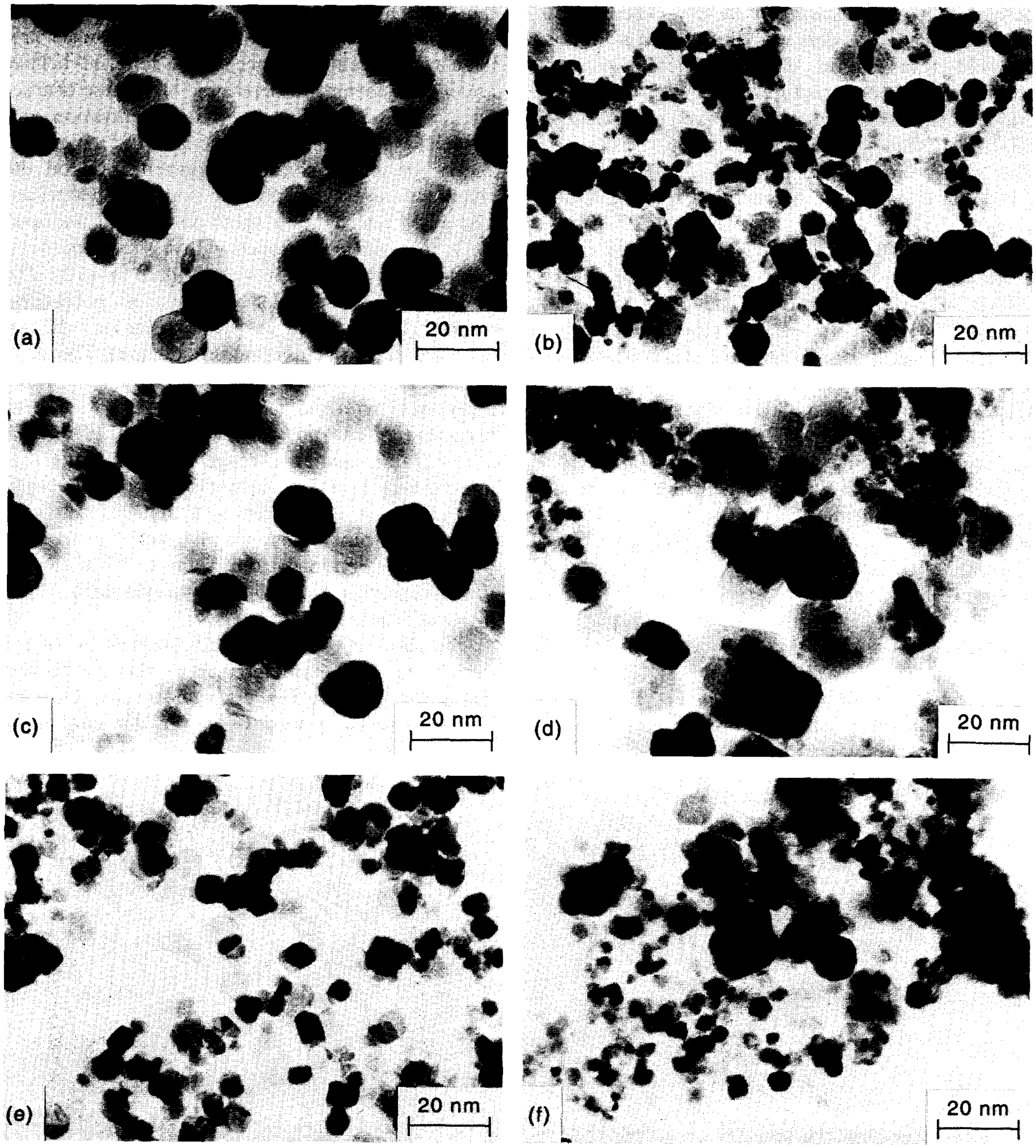

Fig. 2. TEM of the powders prepared under hydrothermal conditions showing (a) the undoped CeO_2 powder and the doped CeO_2 powder containing 6 at% of (b) Mg^{2+}; (c) Ca^{2+}; (d) Sc^{3+}; (e) Nd^{3+} and (f) Y^{3+}.

6 at% of Mg^{2+}, Ca^{2+}, Sc^{3+}, Nd^{3+} and Y^{3+} (b–f) respectively). The undoped powder and the powders doped with Ca^{2+} and Nd^{3+} have a fairly narrow distribution of sizes. However, the powders doped with Mg^{2+}, Sc^{3+} and Y^{3+} have a noticeable bimodal distribution of sizes. The effect of the dopants on the size distribution of the powders is further illustrated in Fig. 3. Particle size distribution histograms determined by measuring maximum diameters of more than 100 particles in TEM micrographs are shown for (a) undoped CeO_2 and CeO_2 doped with (b) 6 at% Ca^{2+} and (c) 6 at% Sc^{3+}. The histogram of the Ca-doped powder is approximately similar to that of the undoped powder. The powder doped with Sc^{3+} has a bimodal distribution of larger particles (average size ≈20 nm) and finer particles (average size ≈8 nm).

The distribution of the dopant in the particles of the powder may also have important conse-

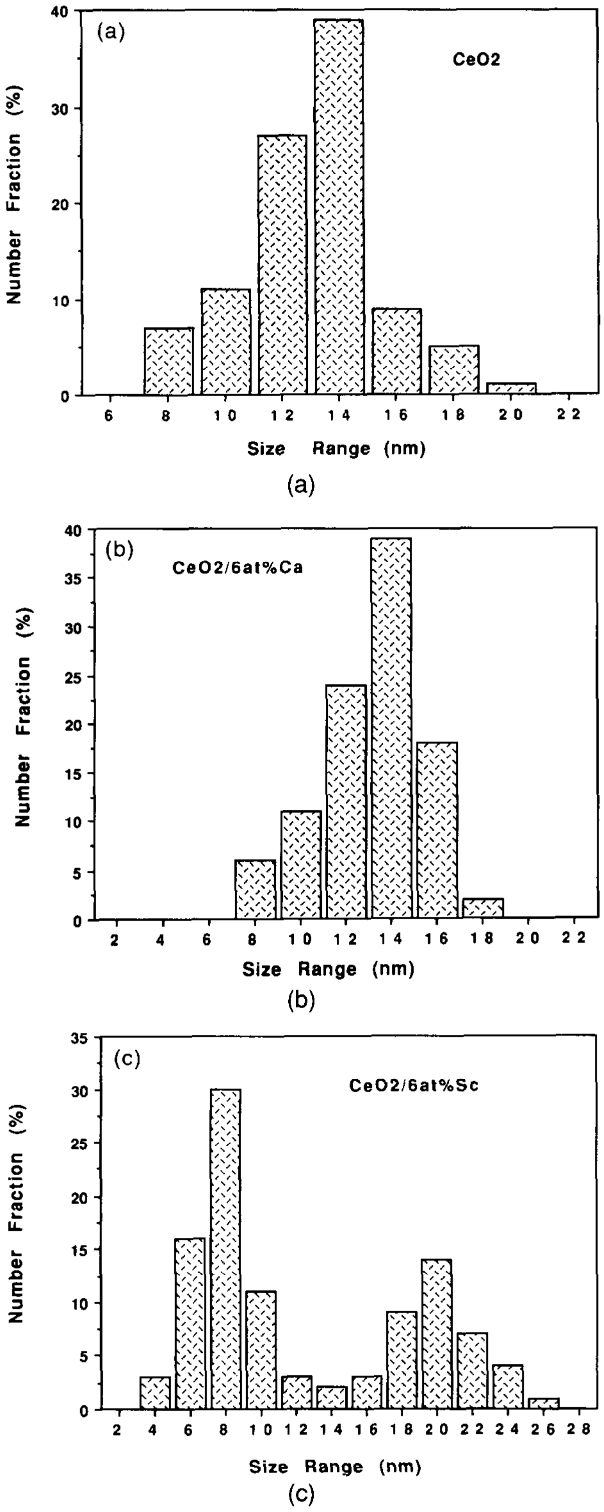

Fig. 3. Histogram showing the particle size distribution of (a) the undoped CeO_2; (b) the CeO_2 powder doped with 6 at% Ca and (c) the CeO_2 powder doped with 6 at% Sc.

quences for sintering. Figure 4 shows high resolution TEM micrographs of the synthesized powder doped with 6 at% Ca^{2+}. The particles are observed to have faceted shapes and, within the limits of resolution, fully crystalline. EDX analysis revealed no difference in the chemical composition of the individual particles. As outlined above, the powders doped with Mg^{2+}, Sc^{3+} and Y^{3+} have a bimodal distribution of sizes. High resolution micrographs

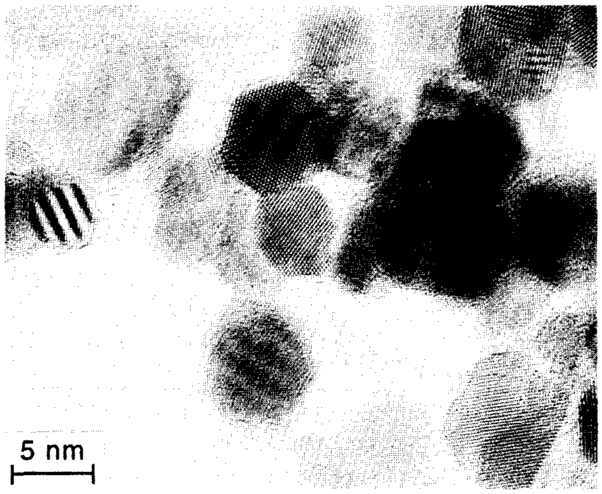

Fig. 4. HREM of the CeO_2 powder doped with 6 at% Ca^{2+}.

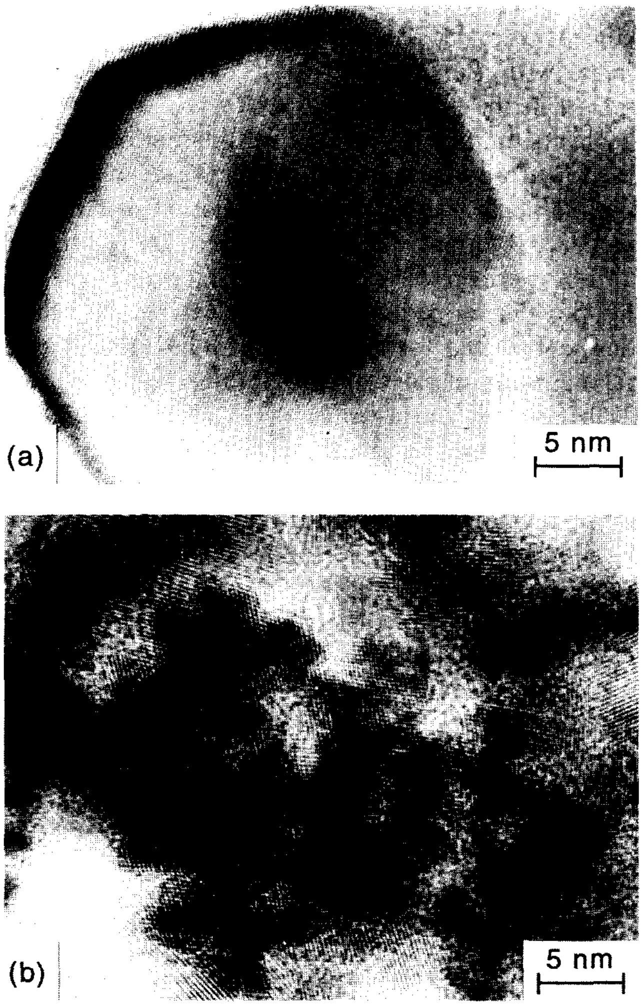

Fig. 5. HREM of the CeO_2 powder doped with 6 at% Y^{3+} showing (a) a larger particle with a lower concentration of Y^{3+} and (b) smaller particles with a higher concentration of Y^{3+}.

of the powder doped with 6 at% Y^{3+} are shown in Fig. 5 for (a) a larger particle and (b) smaller particles in the distribution. The highly crystalline nature of the larger particle is very noticeable. However, for these powders, EDX analysis revealed a significant difference in the dopant

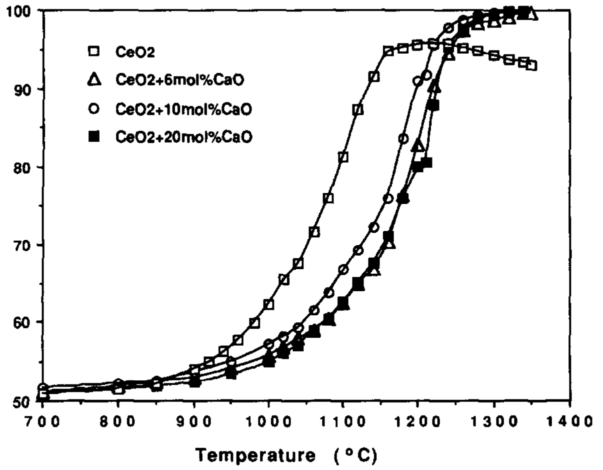

Fig. 6. Relative density versus temperature for the compacted CeO_2 powder doped with 0, 6, 10 and 20 at% Ca^{2+} during sintering at 10°C/min to 1350°C.

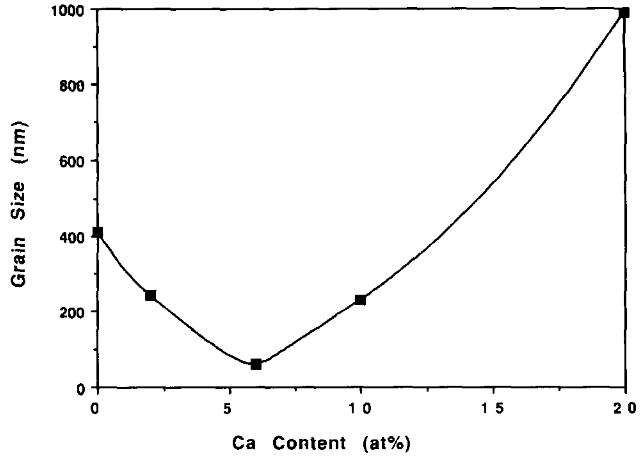

Fig. 7. Grain size versus Ca^{2+} concentration for the powder compacts sintered under identical conditions of 10°C/min to 1350°C.

concentration between the larger and smaller particles, with the concentration being significantly greater in the finer particles.

The sintering curves for the undoped and Ca-doped powders are shown in Fig. 6, where the relative density is plotted as a function of the temperature. Dopant concentrations of 2, 6, 10 and 20 at% were investigated. The sintering curve for the powder doped with 2 at% Ca^{2+} was nearly identical to that for sample doped with 6 at% and, to maintain clarity of the figure, was omitted. Each curve is the average of two runs under the same conditions, and the density at any temperature is reproducible to $\pm 0{\cdot}01$. The sintering behavior of the undoped powder has been described in detail elsewhere.[10] The undoped CeO_2 powder starts to sinter at ≈800–900°C and reaches a density of 0·95 of the theoretical at ≈1200°C, after which the density decreases slightly. It is seen that one effect produced by the dopants is a shift of the sintering curves to higher temperature. Furthermore, the sintering curves for the doped powders lie within a narrow band, which indicates that for the range of values investigated (2–20 at%), the Ca^{2+} concentration has a relatively insignificant effect on the densification. It is also seen that the doped samples reach nearly full density below ≈1300°C.

For the Ca-doped powders, the final grain size of the compacts sintered under identical conditions (10°C/min–1350°C) is shown in Fig. 7 as a function of the dopant concentration. It is seen that the dopant concentration has a significant effect on the final grain size. With increasing Ca^{2+} concentration, the final grain size decreases from ≈400 nm for the undoped sample and reaches a minimum value of ≈30 nm at 6 at%, after which it increases to ≈1 μm for a concentration of 20 at%. SEM of the fracture surfaces of the sintered bodies are shown in Fig. 8. The effect of the Ca concentration on the grain size and microstructure is very striking.

Figure 9 shows the effect of yttrium dopant on the sintering of the compacted powders. Dopant concentrations of 2, 6, 10, 14 and 20 at% were investigated but the data for the powder doped with 14 at% Y^{3+} were omitted to maintain clarity of the figure. As observed above for the powders doped with Ca^{2+}, doping produces a shift in the sintering curves to higher temperature. However, the effect of the Y^{3+} appears to be somewhat more complex than that observed for Ca^{2+}. The shift in the curves increases with increasing Y^{3+} concentration so that higher temperatures are required in order to achieve the same final density. The sintering curve for the sample doped with 20 at% Y^{3+} shows a trend which is different from those of the others. No densification occurs below ≈1300°C, after which the curve increases rapidly. Furthermore, the curve shows a small expansion at ≈1200°C. A small expansion was also observed for the powder doped with 14 at% Y^{3+}. The cause of the expansion is not understood clearly at present. As outlined earlier, X-ray analysis and high resolution electron microscopy show no evidence of free Y_2O_3 in the powders. However, electron microscopy shows that the powder doped with Y^{3+} has a bimodal size distribution and that the smaller particles in the distribution have a higher yttrium concentration (Fig. 5). A possibility is that the expansion is caused by a solid state reaction driven by the yttrium concentration difference between the smaller and larger particles in the powder. After the yttrium concentration has equilibrated, densification occurs rapidly.

The effect of the elemental composition of the dopant on the sinterability of the compacted powders is shown in Figs 10 and 11 for a fixed dopant

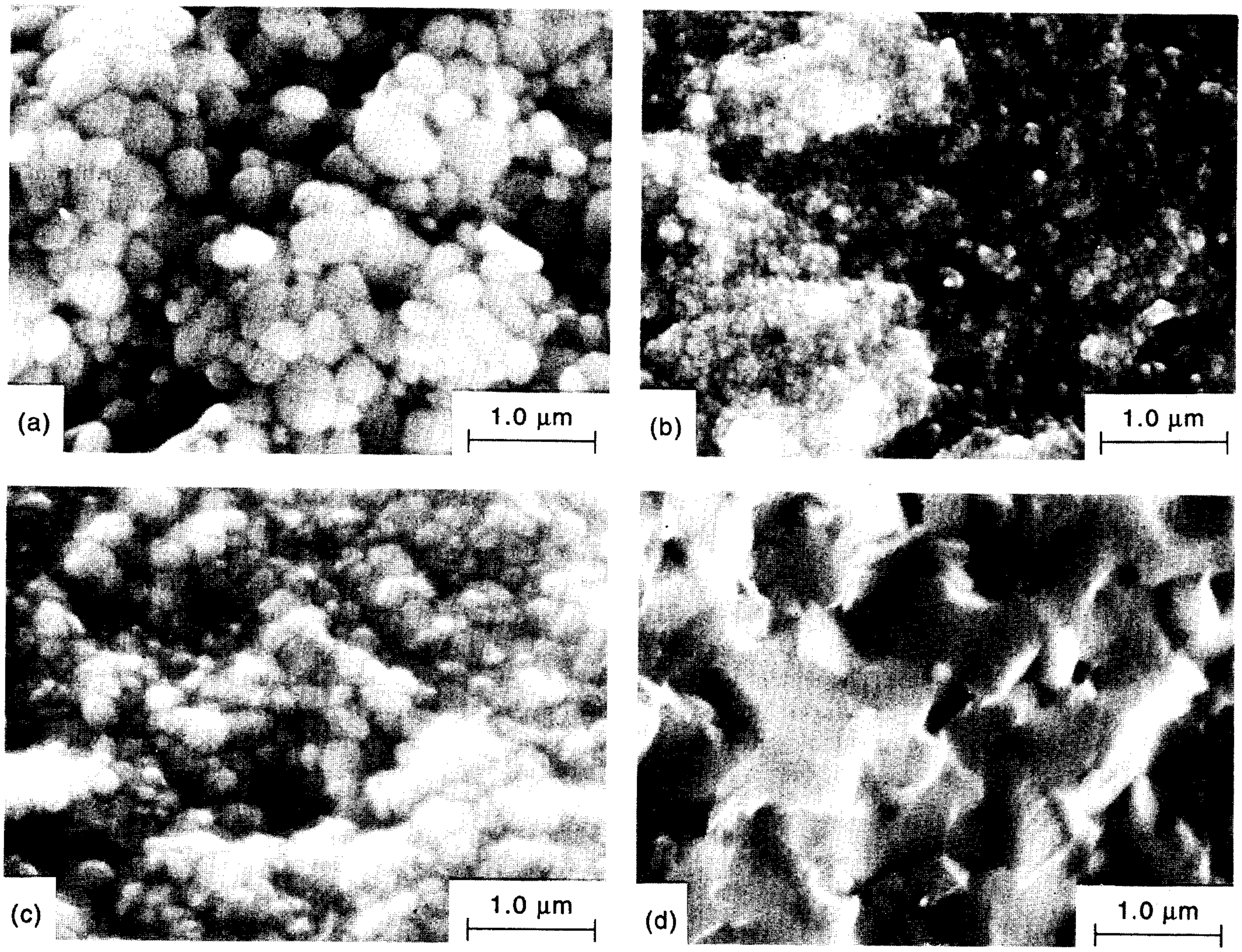

Fig. 8. SEM of the fracture surfaces of the Ca-doped powder compacts after sintering at 10°C/min to 1350°C for Ca^{2+} concentrations of (a) 2; (b) 6; (c) 10 and (d) 20 at%.

concentration of 6 at%. For the divalent cations investigated, i.e. Mg^{2+} and Ca^{2+}, it is seen that both cations lead to a shift of the sintering curve to higher temperature (Fig. 10). However, the final densities obtained under identical sintering conditions are different. The Mg-doped sample reaches a limiting density of ≈95% of the theoretical while the Ca-doped sample reaches almost full density. For the trivalent cations, i.e. Sc^{3+}, Y^{3+} and Nd^{3+}, the shift of the sintering curves to higher temperatures is also observed (Fig. 11).

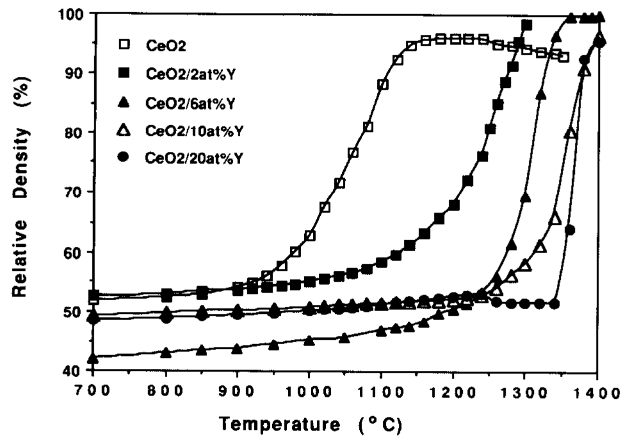

Fig. 9. Relative density versus temperature for the compacted CeO_2 powder doped with 2, 6, 10 and 20 at% Y^{3+} during sintering at 10°C/min.

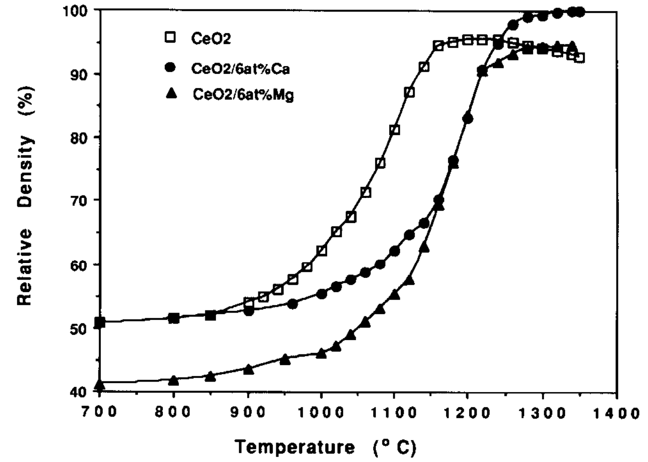

Fig. 10. Relative density versus temperature for the CeO_2 powder compacts doped with 6 at% of the divalent cations, Mg^{2+} and Ca^{2+}, during sintering at 10°C/min to 1350°C. For comparison, the data for the undoped CeO_2 powder compact are also shown.

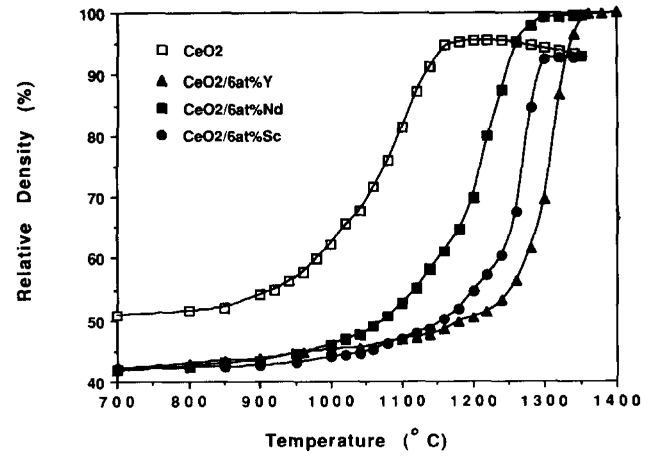

Fig. 11. Relative density versus temperature for the CeO_2 powder compacts doped with 6 at% of the trivalent cations, Sc^{3+}, Y^{3+} and Nd^{3+}, during sintering at 10°C/min. For comparison, the data for the undoped CeO_2 powder compact are also shown.

The extent of the shift is dependent on the elemental composition of the dopant; the smallest shift is caused by Nd^{3+} while Y^{3+} produces the largest shift. As observed for the divalent cations, the final density depends on the elemental composition of the dopant. Almost full density is achieved for the powders doped with Nd^{3+} and Y^{3+} while the powder doped with Sc^{3+} reaches a limiting density of only ≈93% of the theoretical.

SEM of the sintered samples doped with 6 at% of Mg^{2+}, Ca^{2+}, Y^{3+} and Nd^{3+} are shown in Fig. 12. The grain size and microstructure are seen to be highly dependent on the elemental composition of the dopant. Relatively large grain size is obtained with the Mg^{2+} dopant. The microstructure of the Sc-doped sample, not shown here, is close to that for the Mg-doped sample. While Ca^{2+}, Y^{3+} and Nd^{3+} are very effective for achieving small grain sizes, the smallest grain size was obtained for the powders doped with Ca^{2+}.

The sintering behavior of CeO_2 doped with two metal cations, (i.e. double dopants) was also investigated. Figure 13 shows the sintering curves for the compacted powders doped with 3 at% Ca^{2+} + 3 at% Mg^{2+} and 2 at% Ca^{2+} + 4 at% Mg^{2+}. For comparison, the sintering curves for the powders doped with 6 at% Ca^{2+} and with 6 at% Mg^{2+} are also included in the figure. It is seen that while the

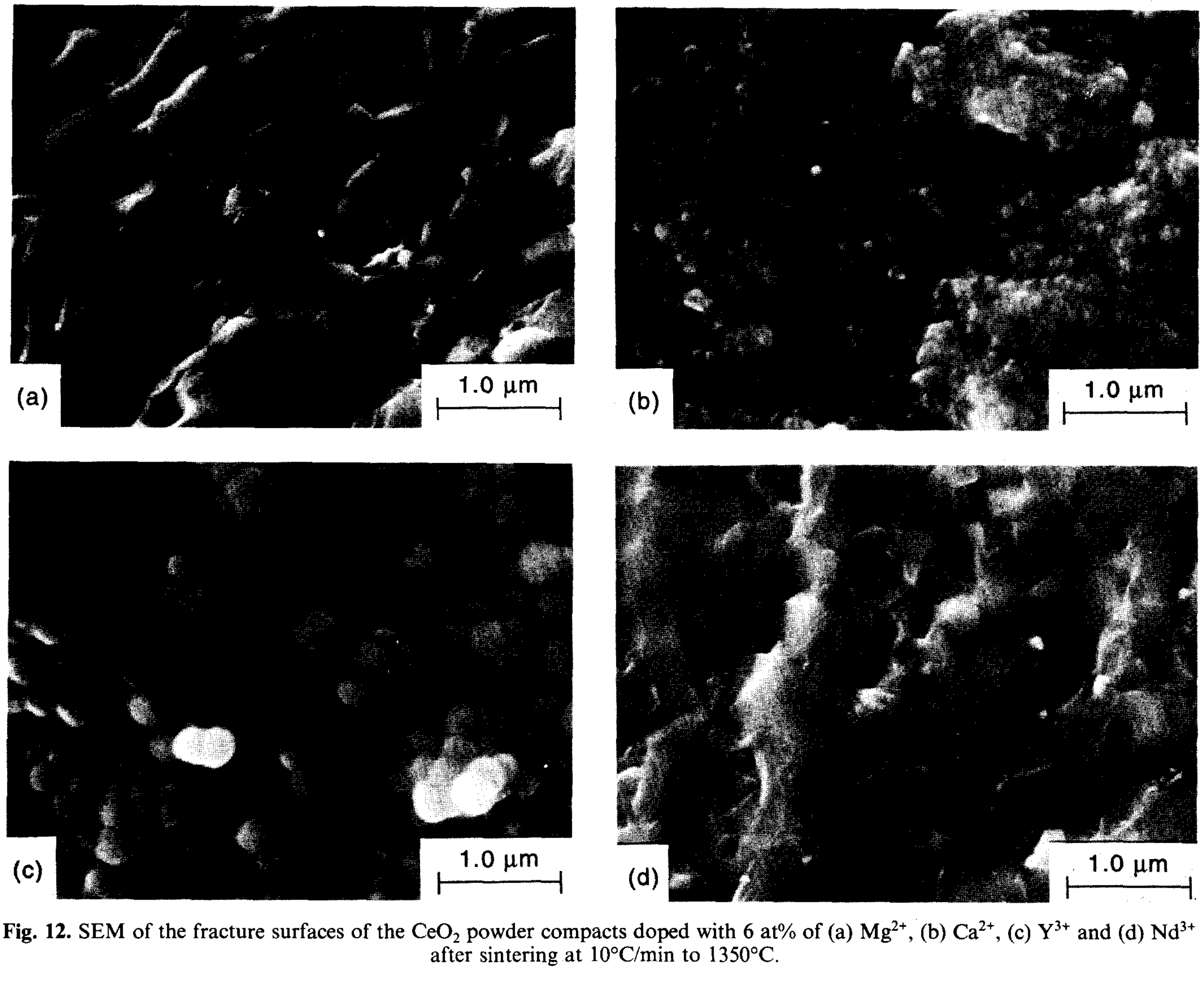

Fig. 12. SEM of the fracture surfaces of the CeO_2 powder compacts doped with 6 at% of (a) Mg^{2+}, (b) Ca^{2+}, (c) Y^{3+} and (d) Nd^{3+} after sintering at 10°C/min to 1350°C.

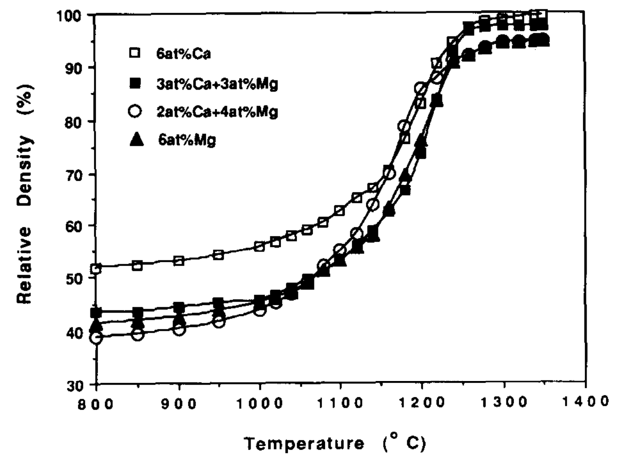

Fig. 13. Relative density versus temperature for the CeO_2 powder compacts doped with double cations, Mg^{2+} + Ca^{2+}, during sintering at 10°C/min to 1350°C. For comparison, the data for CeO_2 powder compacts doped with the single cations at the equivalent concentration are also shown.

green density of the Ca-doped powder compact is somewhat higher than those for the other samples, soon after the onset of densification the data fall within a narrow band. The data therefore indicate that for a fixed concentration of these two dopants, the elemental composition of the dopant does not have a significant effect on the sintering kinetics. The final densities of the doubly-doped samples have values which are intermediate between those for the Mg-doped and Ca-doped samples.

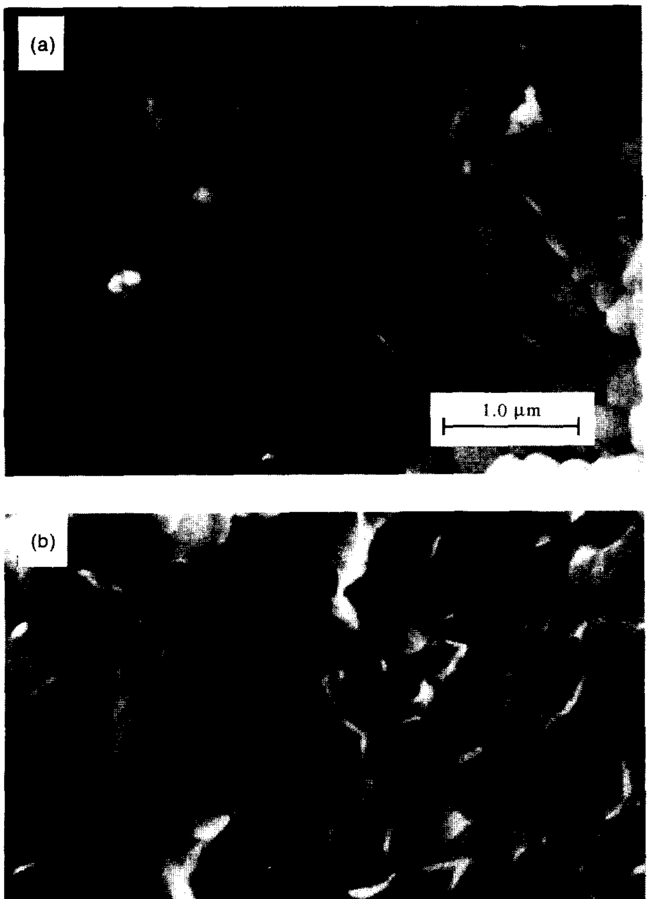

Fig. 14. SEM of the samples described in Fig. 13 containing double dopants of (a) 3at% Ca^{2+} + 3 at% Mg^{2+} and (b) 2 at% Ca^{2+} + 4 at% Mg^{2+}. Part (b) shows the fracture surface of the dense sample but (a) shows the surface of an internal flaw in the dense sample.

Figure 14 shows scanning electron micrographs of the samples containing double dopants after sintering to 1350°C. The micrograph shown in Fig. 14(a) (for the sample doped with 3 at% Ca^{2+} + 3 at% Mg^{2+}) does not represent the true fracture mode of the dense sample. The powder compact used to produce the microstructure contained a small crack (formed during the powder compaction stage). After sintering, the surface of the crack was observed in the SEM. The micrograph reveals a classical microstructure produced by solid state sintering where the flat grain boundaries have clearly developed. Figure 14(b) shows the true fracture surface of the dense sample (containing 2 at% Ca^{2+} + 4 at% Mg^{2+}). The fracture mode is predominantly transgranular. Generally, for the equivalent dopant concentration, the microstructures for the samples containing double dopants show features which are intermediate between those for the Ca-doped sample (Fig. 12(b)) and the Mg-doped sample (Fig. 12(a)).

4 Discussion

The results indicate that the incorporation of dopants produce subtle microstructural effects in CeO_2 powders prepared by hydrothermal processing. The major processes occurring in the hydrothermal technique employed in the present work are the dissolution of an amorphous, gelatinous product and its precipitation in the form of crystalline particles. X-ray diffraction of the powders after the hydrothermal treatment revealed no evidence of free oxides of any of the dopant elements investigated (Mg, Ca, Sc, Y and Nd). Furthermore, high resolution electron microscopy of the doped powders (Figs 4 and 5) revealed that the powders were crystalline in nature. On the basis of the X-ray and electron microscopy data, the dopants may be assumed to be incorporated into the CeO_2 solid solution during the hydrothermal process.

Electron microscopy also indicates that the incorporation of dopants into the CeO_2 powders during hydrothermal synthesis influences the powder morphology and the distribution of the dopant within the powder. Powders doped with Ca^{2+} or Nd^{3+} have a relatively narrow distribution in sizes. Furthermore, EDX analysis of the Ca-doped powder indicates that the chemical composition of the individual particles is the same.

Dopants such as Mg^{2+}, Sc^{3+} and to a lesser extent Y^{3+}, lead to a bimodal distribution of particle sizes. EDX analysis of the powder doped with Y^{3+} also revealed that the dopant concentration was significantly higher in the particles with the smaller sizes. Further work is necessary in order to understand the effect of the dopants on the microstructure and microchemistry of the powders.

The sintering results indicate that the dopants investigated have a profound effect on the densification and grain growth of the compacted powders. All of the dopants lead to a shift in the sintering curve for CeO_2 to higher temperatures (Figs 10 and 11). While the mechanism of densification of CeO_2 is not clear, predictions based on Herring's scaling laws[9] indicate that grain boundary diffusion is enhanced with decreasing particle size. Compared to diffusion through the lattice, grain boundary diffusion is also expected to be more rapid at lower temperatures. For the ultrafine powders and relatively low sintering temperatures used in the present work, it seems reasonable to assume that grain boundary diffusion is the rate-controlling mechanism for densification. The shift in the sintering curves to higher temperatures indicates that the dopants reduce the rate of grain boundary diffusion. This reduction in the grain boundary diffusion, compared to undoped CeO_2, further indicates that the additive cations modify the structure of the grain boundary region.

The dopants were also found to have a dramatic effect on grain growth phenomena during sintering. Dopants can influence the structure of the grain boundary and, hence, the mobility of the grain boundary by two main processes. First, the additive may form a separate phase at the grain boundary by precipitation or by chemical reaction. The second phase can be solid or liquid at the sintering temperature. In the second process, the concentration of the additive cations may be enhanced or diminished in the grain boundary without the formation of a second phase. The term segregation will be used in a limited sense to describe the second process. For the present work, the first process appears unlikely. Detailed microstructural analysis by conventional and high resolution TEM of the sintered Ca-doped sample showed no evidence of a second phase at the grain boundaries (Fig. 15). It will be recalled (Fig. 7) that the Ca-doped samples show the most dramatic change in grain growth behavior. CeO_2 is also known to have a high solid solubility for many dopants, including those investigated in this work.[12-14] Furthermore, the presence of a liquid phase during sintering appears unlikely because of the low final sintering temperature (1350°C) used for most of the experiments in this work.

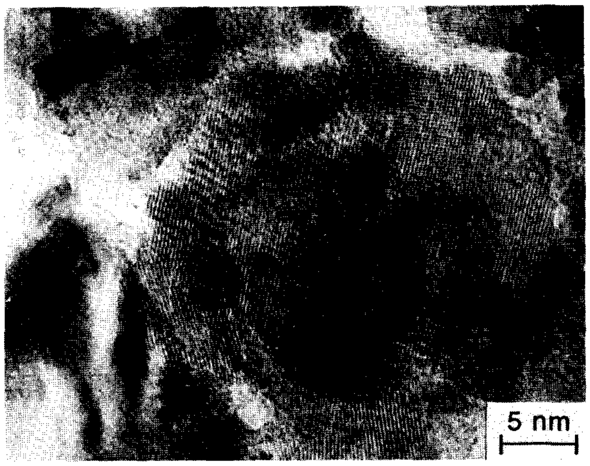

Fig. 15. HREM of a sintered sample of CeO_2 doped with 6 at% Ca^{2+}. The sample was sintered at 10°C/min to 1350°C.

The evidence described above strongly suggests that segregation of the dopants to the grain boundary (referred to as solute segregation) might be an important process by which the dopants influence the sintering and grain growth of CeO_2. The characterization of the microchemistry of the grain boundaries in the sintered samples is currently in progress. However, a number of observations pertinent to the use of solid solution additives in the sintering of ceramics can be made at this stage. One mechanism which is believed to control solute segregation to the grain boundary involves the concept of a space charge.[15-17] It has been shown recently that the effect of dopants on the grain growth of tetragonal zirconia polycrystals (TZP) can be satisfactorily rationalized in terms of the space charge concept.[18] In the space charge theory, surfaces, boundaries and dislocation cores in an ionic crystal may possess a net charge resulting from the presence of excess ions of one type. This charge is compensated by a region of space charge of the opposite sign adjacent to these lattice discontinuities. For ionic crystals doped with aliovalent cations, the magnitude and sign of the space charge are expected to be controlled by the effective charge of the solute. In the present experiments, the dopants present in the bulk of the lattice have a negative effective charge so that, in thermal equilibrium, the boundary will possess a positive charge. The dopants must then segregate to the boundary as a space charge so that the bulk of the crystal remains neutral.

For the aliovalent dopants investigated in this work we may expect, on the basis of the space charge concept, that the divalent cations (Mg^{2+} and Ca^{2+}) are more strongly segregated to the grain boundaries compared to the trivalent cations (Sc^{3+}, Y^{3+} and Nd^{3+}). However, the grain size data show that Ca^{2+}, Y^{3+} and Nd^{3+} are effective for controlling grain growth, with Ca^{2+} being the most effective, while Mg^{2+} and Sc^{3+} are not effective. The grain size data cannot therefore be rationalized in terms of the space charge concept only.

An interaction between the moving grain boundary and the dopant cations can also originate from the strain energy caused by the mismatch in size between the dopant cations and the host cations.[19] Because of the size mismatch, there will be a difference in strain energy between a dopant cation situated at or near the grain boundary and one in the crystal lattice. For aliovalent dopants, the interaction between the strain field and the boundary must be coupled with the space charge field because of the effective charge of the dopant cations. The distribution of the dopant cations and defects within the space charge cloud can therefore be significantly affected by the strain field due to the size mismatch.

Assuming eight-fold coordination, the ionic radii of Ce^{4+}, Mg^{2+}, Ca^{2+}, Sc^{3+}, Y^{3+} and Nd^{3+} are 0·097, 0·089, 0·112, 0·087, 0·102 and 0·112 nm, respectively.[20] The cations Mg^{2+} and Sc^{3+} which have ionic radii smaller than that of host Ce^{4+} ion, (i.e. the undersize cations) are not effective for grain growth control while Ca^{2+}, Y^{3+} and Nd^{3+} with ionic radii larger than that of the Ce^{4+} ion, (i.e. the oversize cations) are effective for grain growth control. For the oversize cations, Ca^{2+} with the highest effective charge is most effective for grain growth control. It is clear that both the charge and the size mismatch of the dopant cations are important factors for grain growth control by divalent and trivalent cations.

Assuming that the segregated dopants control the grain boundary mobility by the solute drag mechanism proposed by Cahn,[21] the mobility of the grain boundary is given approximately by an equation of the form:

$$M = \frac{D}{\Delta C kT} \qquad (3)$$

where D is the diffusivity of the dopant cation, ΔC is the excess concentration of the dopant cation in the grain boundary, k is the Boltzmann constant and T is the absolute temperature. Taking the case of the divalent dopants, the effectiveness of Ca^{2+}, compared to Mg^{2+}, for grain growth control may be due to an increased segregation to the grain boundary due to a larger size mismatch or a decrease in the diffusivity of the dopant due to its larger ionic radius or a combination of the two. The concentration of the dopants in the grain boundary is currently being investigated. However, the effectiveness of the Ca^{2+} dopant, compared to Mg^{2+}, can be rationalized in terms of its larger ionic size. For cations of nearly the same size, e.g. Ca^{2+} and Nd^{3+}, the greater effectiveness of Ca^{2+} can be rationalized in terms of its greater effective charge. Thus, based on the space charge concept and the strain mismatch, Ca^{2+} is expected to be most effective for grain size control, as is observed.

For Ca^{2+} which forms the most effective dopant for grain growth control, the data of Fig. 7 for the grain size after identical sintering conditions show that the concentration of the dopant has a significant effect on the grain size. The variation of the grain size with dopant concentration is not uniform. With increasing Ca^{2+} concentration, the grain size decreases monotonically and reaches a minimum at ≈5–6 at%, after which it increases monotonically. There is therefore an optimum Ca^{2+} concentration which is most effective for grain growth control. Grain size data for the CeO_2 doped with Y^{3+} also reveal an optimum dopant concentration for grain growth control at ≈6 at%. As outlined earlier, high resolution TEM of the sintered body doped with 6 at% Ca^{2+} did not reveal the presence of a discrete second phase at the grain boundaries. For samples containing low concentrations of dopants, (e.g. below the optimum concentration of ≈6 at%), the grain growth behavior can be rationalized in terms of the solute drag mechanism. However, the mechanism cannot be used to explain the grain growth behavior at large dopant concentrations where the grain size of the doped samples are greater than that for the undoped CeO_2 (Fig. 7).

For the same concentration of dopants (6 at%), the data indicate that the effect of double dopants (Mg^{2+} + Ca^{2+}) on the sintering and grain growth is intermediate between those of the single dopants. Under identical sintering conditions, the grain size for the sample doped with 3 at% Mg^{2+} + 3 at% Ca^{2+} is ≈0·5 μm which is approximately half-way between those for the samples doped with 6 at% Mg^{2+} and 6 at% Ca^{2+} (≈30 nm) but approximately twice that for the sample doped with 3 at% Ca^{2+} (200 nm). Both Mg^{2+} and Ca^{2+} are expected to substitute at the regular Ce^{4+} lattice sites and the nature of the charged defects produced by Mg^{2+} and Ca^{2+} substitution is therefore expected to be the same. Compensation of one type of defect by another cannot occur for the double dopants used in this study. The data for the double dopants therefore indicate that the dopants act to influence the grain boundary structure.

5 Conclusions

Divalent and trivalent dopants (Mg^{2+}, Ca^{2+}, Sc^{3+}, Y^{3+} and Nd^{3+}) produced subtle changes in the microstructure and microchemistry of ultra-fine

CeO_2 powders prepared under hydrothermal conditions. The powders doped with Mg^{2+}, Sc^{3+} and, to a lesser extent Y^{3+}, had a bimodal size distribution. EDX analysis of the Y-doped powder showed that the dopant concentration was significantly higher in the smaller particles. The undoped powder and the Ca-doped and Nd-doped powders had a fairly narrow size distribution. For the Ca-doped powder, no difference in the chemical composition of the individual particles was detected by EDX analysis.

The dopants had a dramatic effect on the sintering and grain growth behavior of the compacted powders. Compared to the undoped CeO_2, all of the dopants produced a shift in the sintering curve to higher temperature. The effect of the dopants on grain growth was dependent on both the cation charge and the cation radius. The undersize cations, Mg^{2+} and Sc^{3+} were not effective for grain growth control. Grain growth was suppressed in the samples doped with the oversize cations, Ca^{2+}, Nd^{3+} and Y^{3+}, with Ca^{2+} being the most effective for grain growth control.

At low concentrations, the influence of the dopants on the sintering and grain growth behavior can be rationalized in terms of segregation to the grain boundary by a space charge mechanism and solute drag on the grain boundary. However, this mechanism cannot explain the enhanced grain growth at large dopant concentrations where the grain size of the doped sample is significantly greater than that for the undoped CeO_2.

References

1. Gleiter, H., Nanocrystalline materials, *Prog. Mater. Sci.*, **33**(4) (1989) 223–315.
2. Birringer, R., Gleiter, H., Klein, H.-P., & Marquard, P., Nanocrystalline materials: an approach to a novel solid structure with gas-like disorder, *Phys. Lett.*, **102A** (1984) 365–9.
3. Hahn, H., Logas, J. & Averback, R. S., Sintering characteristics of nanocrystalline TiO_2, *J. Mater. Res.*, **5**(3) (1990) 609–14.
4. Mayo, M. J., Siegel, R. W., Narayanasamy, A. & Nix, W. D., Mechanical properties of nanophase TiO_2 as determined by nanoindentation, *J. Mater. Res.*, **5**(5) (1990) 1073–82.
5. Nieman, G. W., Weertman, J. R. & Siegel, R. W., Mechanical behavior of nanocrystalline Cu and Pd, *J. Mater. Res.*, **6**(5) (1991) 1012–27.
6. Komarneni, S., Roy, R., Breval, E., Ollinen, M. & Suwa, Y., Hydrothermal route to ultrafine powders utilizing single and diphasic gels, *Adv. Ceram. Mater.*, **1**(1) (1986) 87–92.
7. Komarneni, S., Fregeau, E., Breval, E. & Roy. R., Hydrothermal preparation of ultrafine ferrites and their sintering, *J. Am. Ceram. Soc.*, **71**(1) (1988) C26–8.
8. Somiya, S., Yoshimura, M., Nakai, Z., Hishinuma, K. & Kumaki, T., Hydrothermal processing of ultra-fine single-crystal zirconia and hafnia powders with homogeneous dopants, *Advances in Ceramics*, **21** (1987) 43–55.
9. Herring, C., Effect of change of scale on sintering phenomena, *J. Appl. Phys.*, **21** (1950) 301–3.
10. Zhou, Y. C. & Rahaman, M. N., Hydrothermal synthesis and sintering of ultrafine CeO_2 powders, *J. Mater. Res.*, **8**(7) (1993) 1680–6.
11. Blumental, R. N., Brugner, F. S. & Garnier, J. E., The electrical conductivity of CaO-doped nonstoichiometric cerium oxide from 700 to 1500°C, *J. Electrochem. Soc.*, **120** (1973) 1230–5.
12. Distine, R. T., Blumenthal, R. N. & Kuech, T. F., Ionic conductivity of calcia, yttria, and rare earth-doped cerium oxide, *J. Electrochem. Soc.*, **126**(2) (1979) 264–9.
13. Yahiro, H., Eguchi, K. & Arai, H., Electrical properties and reducibilities of ceria–rare earth oxide systems and their application to solid oxide fuel cell, *Solid State Ionics*, **36** (1989) 71–5.
14. Yahiro, H., Ohuchi, T., Eguchi, K. & Arai, H., Electrical properties and microstructure in the system ceria–alkaline earth oxide, *J. Mater. Sci.*, **23** (1988) 1036–41.
15. Kingery, W. D., Plausible concepts necessary and sufficient for interpretation of ceramic grain boundary phenomena: I. grain-boundary characteristics, structure, and electrostatic potential, *J. Am. Ceram. Soc.*, **57**(1) (1974) 1–8; II. solute segregation, grain-boundary diffusion, and general discussion, *J. Am. Ceram. Soc.*, **57**(2) (1974) 74–83.
16. Lehovec, K., Space charge layer and distribution of lattice defects at the surface of ionic crystals, *J. Chem. Phys.*, **21** (1953) 1123–8.
17. Frenkel, J., *Kinetic theory of liquids*, Oxford University Press, New York, NY, 1946, p. 36.
18. Hwang, S.-L. & Chen, I-W., Grain size control of tetragonal zirconia polycrystals using the space charge concept, *J. Am. Ceram. Soc.*, **73**(11) (1990) 3269–77.
19. Yan, M. F., Cannon, R. M. & Bowen, H. K., Grain boundary migration in ceramics, Ceramic Microstructures '76. Eds R. M. Fulrath & J. A. Pask. Westview Press, Boulder, CO, 1977, pp. 276–307.
20. Shannon, R. D., Revised effective ionic radii and systematic studies of inteatomic distances, halides and chalcogenides, *Acta Crystallogr.*, **A32** (1976) 756.
21. Cahn, J. W., The impurity drag effect in grain boundary motion, *Acta Metall.*, **10**(9) (1962) 789–98.